Finding mineralogically interesting targets for exploration from spatially coarse visible and near IR spectra

Leah H. Roach [a,*], John Mustard [a], Aline Gendrin [a], David Fernández-Remolar [b], Ricardo Amils [b,c], Linda Amaral-Zettler [d]

[a] *Department of Geological Sciences, Box 1846, Brown University, Providence, RI 02912, USA*
[b] *Centro de Astrobiología, INTA-CSIC, Ctra Ajalvir km. 4, 28850 Torrejón de Ardoz, Spain*
[c] *Centro de Biología Molecular, CSIC-UAM, Cantoblanco, 28049 Madrid, Spain*
[d] *The Bay Paul Center, Marine Biological Laboratory, USA*

Abstract

Spectroscopic studies of analog terrestrial mineral assemblages are necessary to develop criteria to identify similar environments on Mars. We use visible/near infrared (VNIR) laboratory, field, and remotely acquired spectral data to identify the iron-bearing and hydrous minerals of Rio Tinto, Spain, an astrobiological analog. Mineralogy evolves from iron sulfate- and oxide-rich (jarosite, rozenite, gypsum, schwertmannite, copiapite, goethite, and hematite assemblages) in young sediments to hydrated iron oxides in preserved terraces.

Using spectra from the Rio Tinto, we examine one of the key challenges of extraterrestrial exploration: how to identify promising targets from spatially coarse data for in situ investigation. We apply an index to quantify the expression of spectral diversity as a function of spatial scale from hand sample to landscape. To validate this method for use at the decimeter orbital scale, we apply the index to cm-scale point spectra and meter-scale gridded spectra collected in the field. This exercise in spatial scaling gives increased confidence in the ability of the Spectral Variance Index (SVI) method to locate regions with increased mineral diversity from remotely sensed data. We divide the remotely sensed data into 25×25 pixel ($200\,m \times 200\,m$) cells and calculate the average mean (albedo) and spectral variance over all wavelengths for each cell. We next calculate the expected variance for each cell with a linear regression between mean and spectral variance. The number of standard deviations of each cell's spectral variance is from the expected variance is the SVI value. We locate ~ 20 areas with high SVI values within the tailing piles and along wide riverbanks downstream of the active mine. This method uses spatially coarse VNIR spectra to recognize areas in Rio Tinto that would be ideal targets for future field exploration, and could also be applied to Mars orbital spectral datasets, such as OMEGA and CRISM.
© 2006 Elsevier B.V. All rights reserved.

1. Introduction

Rio Tinto, Spain is a biologically active extreme environment whose chemolithotrophic ecosystem is an established astrobiological analog for Mars. Chemolithotrophic

* Corresponding author. Tel.: +1 401 863 3485.
  E-mail address: Leah_Hutchison@brown.edu (L.H. Roach).

microorganisms such as *Acidithiobacillus ferrooxidans* and *Leptospirillum ferrooxidans* control the cyclic oxidation and reduction of iron and sulfur, maintaining the extremely low pH and high Fe^{3+} concentration in the stream [1,2]. The high metal concentration and pH <3.0 due to iron buffering and biologically accelerated iron cycling sustain a variety of prokaryotic and eukaryotic microorganisms [3] that flourish in biofilms along the Rio Tinto riverbed. In addition to being a focus of astrobiological research, the Rio Tinto has been studied to understand its geo–bio interactions [1,2,4], geologic history [4–6] and mineralogy [5,7–9]. The ancient and modern geologic deposits allow the study of depositional and diagenetic processes in this iron- and sulfur driven environment [4,5], which contain a diverse mineralogy consisting of hydrated ferrous sulfates, mixed ferrous/ferric hydroxysulfates, and iron oxides [7].

The iron oxide and sulfate mineralogy of the Rio Tinto is compelling in the light of new observations on Mars. The Thermal Emission Spectrometer (TES), Mars Exploration Rovers (MER), and the Observatoire pour la Minéralogie, l'Eau, les Glaces, et l'Activité (OMEGA) instruments have revealed a diverse combination of mafic silicates with localized occurrences of iron oxides, hydrated sulfates and phyllosilicates [10–14]. The regional occurrences of these sulfate and phyllosilicate-bearing materials help constrain the local geochemical evolution and our understanding of possible habitable environments on Mars. Rio Tinto presents less a specific analog to Mars and more model system in which particular minerals and their distribution can be studied on a variety of scales. As a model system, Rio Tinto has the potential to explain some of the martian geologic and mineralogic observations and provides necessary ground truth for recognizing and exploring such habitats on Mars.

The goals of this paper are to develop an exploration strategy for iron oxide and sulfate-rich environments over a range of spatial scales. The three scales of exploration – orbital, landscape, and hand sample – have increasing ability to distinguish mineralogy and decreasing ability to put mineralogy within a geologic context. The Rio Tinto is a good example of the balance that is sought between local mineralogy and geology, as the headwaters that exhibit important biological and mineralogical diversity are very small and difficult to fully characterize from orbit. We define the remote sensing signatures of the diverse iron oxide, hydrated sulfate and silicate mineralogy of Rio Tinto and develop exploration criteria to recognize these compelling targets from remotely sensed data.

The challenge when presented with large quantities of remotely sensed data is to determine which areas warrant further detailed investigation. There are several ways to address this challenge. The first is to create global maps of minerals or mineral indicators from orbit, using coarse spatial resolution data. While global maps define the likely presence of minerals, they do not necessarily identify mineral collections. Another strategy is to identify the most extreme or diverse spectral types (Pixel Purity Index [15], etc.) under the assumption that these rare occurrences are associated with key environments. While this approach is excellent to identify the range of mineralogy present, it does not necessarily identify where diverse mineral mixing exists. A third method, spectral variance, is a new concept blending spatial and spectral components to identify localized areas with diverse mineralogic assemblages. We apply a spectral variance index, based on the work of Martínez-Alonso [16], to locate mineralogically interesting areas from spatially coarse spectra.

2. Mineralogy of study site

The Rio Tinto is a 100-km long, heavy metal rich river in southwest Spain whose source lies in one of the world's largest pyritic (FeS_2) belts (Fig. 1). Pyrite oxidation, accelerated by microbes capable of aerobic iron and sulfur oxidation and anaerobic iron reduction, releases ferric iron and heavy metals into the groundwater [1]. A wide array of iron- and sulfur-bearing minerals exist at Rio Tinto because of the high SO_4^{2-} and Fe^{3+} concentrations supplied from acidic groundwater transported along secondary faults intersecting subsurface habitats [17]. Fernandez-Remolar et al. [4] have identified gypsum, copiapite group, hydronium jarosite, natrojarosite, rozenite, epsomite, hexahydrite, alunogen, and barite as efflorescent precipitates that line stream margins. The mineralogy along the stream banks also evolves with diagenesis as is shown in the three abandoned riverbank terraces. The oldest terrace has an absolute age of 2.1 Ma while the other two ranges approximately from Pleistocene to Holocene from stratigraphic relationships [4]. Comparison of sediments from active fluvial deposits and lithified ironstones from the three abandoned river terraces shows how the diverse iron oxide and hydrated mineral combinations change into sulfur-poor hematite and goethite during diagenesis.

3. Approach

Our goal is to understand how the spectral signatures of iron oxide and sulfate mineral mixtures present at the

Fig. 1. Context map of Rio Tinto source region showing the location of the river, its source in Peña de Hierro, and sampling locations in three source springs (Origin, Angeles, Anabel's Garden), three river terraces (youngest, intermediate, and oldest), and four tailings piles (ochre, gray, and black tailings and a road cut near the railroad station). The youngest terrace is off the map, a couple of km south along the river. The nearby towns of Nerva and Rio Tinto are shown for context. The white box delineates the region of the lake used to estimate noise in the data.

Rio Tinto change with spatial scale. We identify the iron oxide and sulfate mineralogy on the scale of the hand sample. To compare that cm-scale understanding of mineralogy to landscapes with complex mineral mixtures, we examine spatial variations in mineralogy using a dataset of intermediate spatial resolution (1 m). At even larger spatial resolution, mineral mixtures complicate unique mineral determination. In this case, we apply the spectral variance index method to locate areas of high metal diversity without quantifying the mineralogy present. These mineralogically diverse areas would be scientifically interesting locations for future exploration. We treat the field, laboratory, and remotely acquired spectra separately.

4. Laboratory spectra

Samples collected on January 11–16, 2005 from the source springs, soils, tailings and terraces were mea-

sured using the Nicolet Nexus 870 Fourier transform infrared (FTIR) spectrometer fitted with a Pike Technologies biconical attachment (AutoDiff™) in the Reflectance Experiment Laboratory (RELAB) at Brown University [18–20]. FTIR spectra were measured relative to a rough gold standard over the wavelength range 1.66–25.0 μm at a spectral resolution of $4 \, cm^{-1}$ in a CO_2- and H_2O-purged environment. Spectra were also measured using the RELAB bidirectional spectrometer ($i=30°$, $e=0°$) over the wavelength range 0.32–2.55 μm at a sampling of 10 nm under ambient conditions. All FTIR spectra were scaled to the maximum reflectance point of their corresponding bidirectional spectra and were spliced with the bidirectional spectra near 1.8 μm. This scaling is because the bidirectional spectrometer is well calibrated and gives "absolute" reflectance [18,19].

Lithified iron oxide samples from the terraces were measured as fresh and weathered-surface chips as well
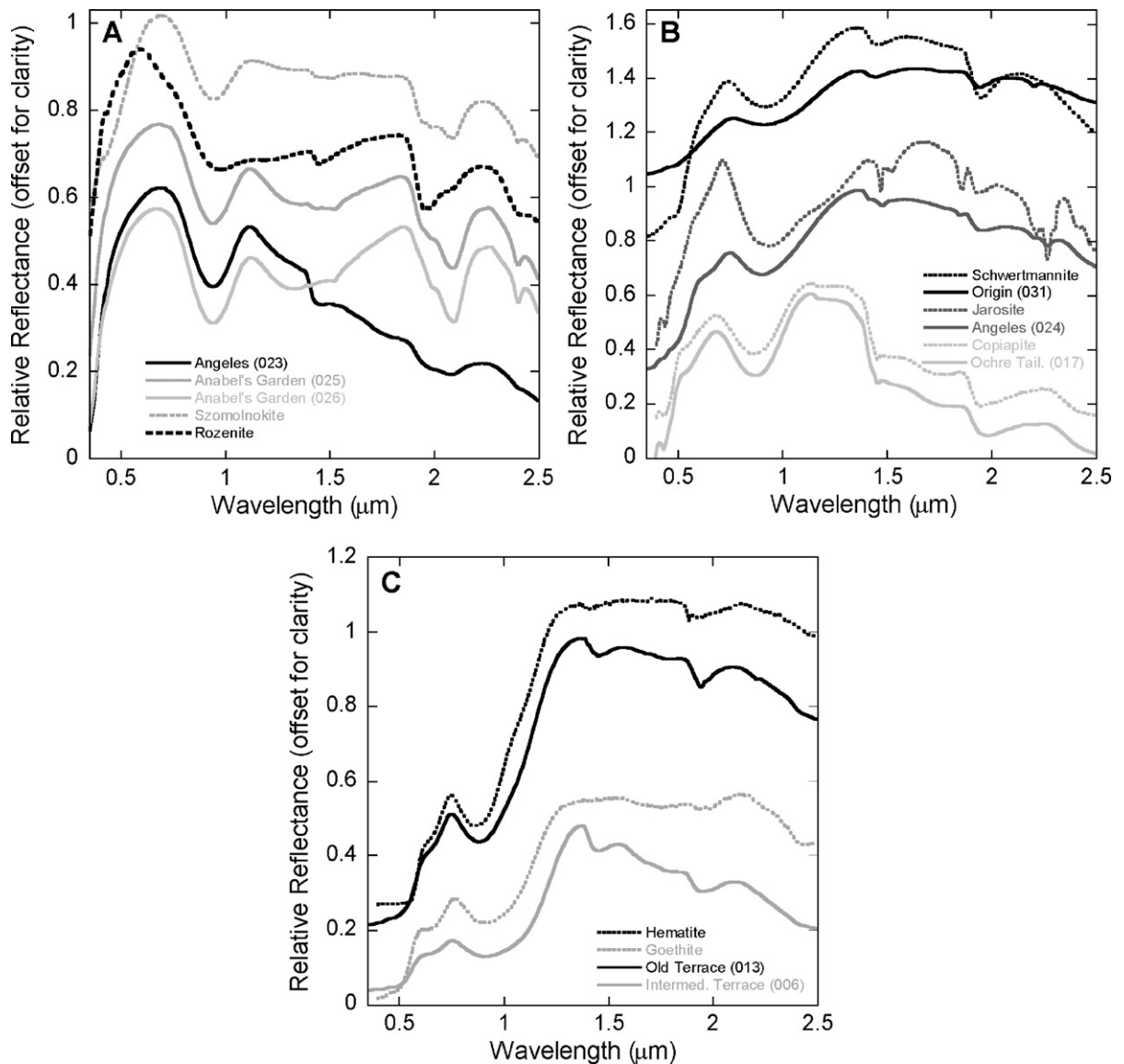
Fig. 2. Representative laboratory spectra of (a) hydrated iron sulfates, (b) hydroxylated iron sulfates, and (C) iron oxides identified from ancient terraces and modern soils and efflorescent deposits. Library spectra in (A) schwertmannite CJB130 [29,35], jarosite LASF27A and copiapite LASF31A; (B) szomolnokite JB622A and rozenite JB626B [29,35]; (c) hematite LAHE01A and goethite WS220.

as <250 and >250 μm size fractions. Samples were ground with mortar and pestle and sieved to the appropriate size fraction. Powdery sulfate-rich samples were measured as bulk materials whereas soil samples were dry sieved to <250 μm without grinding (Fig. 2).

Mineral identification comes from comparison of laboratory spectra of field samples with the crystal field transitions, charge transfers, and vibrational features observed in the RELAB and USGS spectral libraries [21] and published spectra [e.g. 22].

4.1. Elemental abundance method

We measure elemental abundance with two techniques: by inductively coupled plasma (ICP) emission spectroscopy and with an elemental analyzer. JY2000 Ultrace ICP atomic emission spectroscopy is capable of measuring the abundance of most nonvolatile elements with atomic weights greater than 10. We dissolve the samples in an acid solution and measure it in the ICP spectrometer by typical methods. Since the fusing

temperature used in preparing samples for the ICP emission spectrometer is sufficiently high to burn off the most volatile elements, we quantify those volatile elements using the elemental analyzer. The CE Instruments Model NC2100 elemental analyzer can measure the mass abundance of C, N, and S in a finely ground sample.

4.2. Mineral identification results

VNIR reflectance spectra (0.4–2.5 µm) of modern and ancient sediments at Rio Tinto display the entire range of iron sulfate-oxide maturity (Fig. 2) [7,23]. Mineral mixtures complicate identification but can be partially deconvolved by looking for vibrational features and crystal field transitions in mineralogically diagnostic wavelength regions.

Hydrated ferrous sulfates such as szomolnokite (or a combination with other Fe^{2+} sulfates) (Fig. 2A) were identified based on similarity to spectra from Bishop et al. [24]. These Fe^{2+} sulfates were found at several source springs (Anabel's Garden and Angeles) where they formed near stream edges by capillarity [4]. Identifying the hydration state of Fe^{2+} sulfates in the field is difficult since they are often in mixed hydration states and can easily convert between states with change in humidity [25].

Ferrous sulfates oxidize and dehydroxylate over time into mixed ferrous/ferric sulfates with less structural water [26]. We identify hydroxylated sulfates (Fig. 2B) such as jarosite, copiapite group members, and schwertmannite. Hydrated Fe^{2+}/Fe^{3+} sulfates of the copiapite group have similar spectra; this ambiguity makes VNIR spectral identification of individual copiapite group members of secondary utility to elemental determination through XRD or Mössbauer spectroscopy. Fernández-Remolar et al. [4] have performed XRD on Rio Tinto samples (from similar locations as used in this analysis) and identified various copiapite group minerals. Schwertmannite (Fig. 2B) is a good spectral analog, but not a unique identification, for sample Origin #31, a colloidal film on the surface of the Origin spring [25]. Schwertmannite is a less soluble hydroxysulfate mineral that is a common phase with jarosite in ochre deposits from acid sulfate solutions [26]. Previous XRD work found schwertmannite concentrated in the last ferric precipitates of evaporated pools during the dry season [4]. However, it is difficult to confidently identify using XRD because it is poorly crystalline, metastable and commonly admixed with other nanophase Fe minerals [26].

Mixed valence iron sulfates continue to mature and hydrolyze to oxyhydroxysulfates and eventually leach to become iron oxides and hydroxides [26]. Goethite, hematite and iron oxide mixtures (Fig. 2C) were identified in the recent soils and all three terraces. Gypsum was frequently found in mixtures with iron oxides. In addition to the iron oxides and sulfates identified in the recent sediments and abandoned terraces, absorptions in the 2 µm region indicate phyllosilicates were present at many sites. The phyllosilicates are related to the acidic weathering of feldspars and are transported to the river during rainfall events. We mention this mineral identification for completeness but do not discuss clay minerals further as they are minor minerals in the sedimentary history of the river.

4.3. Elemental abundance results

The goethite and hematite-rich terrace samples show absorptions at 1.4 and 1.9 µm and a generally negative slope at wavelengths >1.3 µm (Fig. 2C) that could be interpreted as due to hydroxyl-containing minerals such as sulfates or phyllosilicates. To test the presence of sulfates, sample mineralogy was partially resolved by elemental and stepped dehydration studies. Results from the elemental analyzer and ICP emission spectrometer for each of the terraces (Table 1) show too little S for admixed hydrated sulfates to be the minerals causing those absorption features; water alone can explain the absorption features near 1.4 and 1.9 µm.

5. Field spectra

We collected spectra in a 20 m × 20 m grid pattern at Anabel's Garden, one of the most mineralogically diverse sites in the Rio Tinto headwaters, to understand spatial mineral distribution at the landscape scale. VNIR

Table 1
Percent elemental abundance in the oldest, intermediate and youngest terraces of Rio Tinto. N, C and S determined by elemental analyzer; Al, Ca, Fe, K, Mg, Na, P and Si by ICP emission spectroscopy

Location	Al %	Ca %	Fe %	K %	Mg %	Na %	P %	Si %	N %	C %	S %	Total %
Oldest	0.54	0.1	43.9	0.03	0.01	0.01	0.03	0.65	0.04	0.19	0.4	45.9
Intermed.	0.92	0.04	55.1	0.05	0.02	0.01	0.06	0.8	0.03	0.18	0.51	57.72
Youngest	1.74	0.13	31.4	0.62	0.1	0.26	0.05	16.8	0.07	0.5	3.4	55.07

Trace elements such as Ba, Mg and Sr have been omitted. Volatile elements, such as O, make up the bulk of the missing mass.
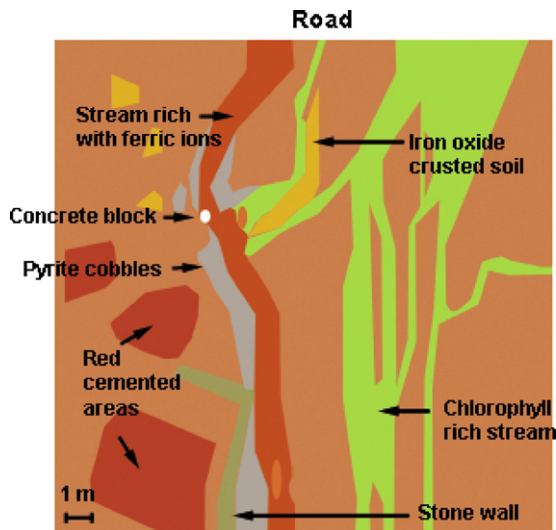
Fig. 3. Map of Anabel's Garden. The streams with different physiochemical parameters run adjacent to each other. Some evidence of the substantial human influence on this environment is visible in the cement cinder block near the intersection of the two streams and the ground-level stone wall. The area was divided into a 20 m × 20 m sampling grid with 1 m spacing, for a total of 400 spectra. The grid center is located at (37.7349 N, 6.5602 E).

spectra were measured in the field with a portable ASD FieldSpec FR spectrometer referenced to Spectralon® to produce reflectance spectra and then converted to absolute reflectance using RELAB measurements of the Spectralon® panel. Anabel's Garden is an ideal location to explore the spatial relationships between mineralogy and stream chemistry as it has two separate springs with different physiochemical parameters that run parallel for 10 m before mixing. The 20 m × 20 m square grid (Fig. 3) was marked off in 1-m increments and 400 spectra with 18° FOV optics (15 cm radius or 700 cm^2 spot size from a height of 1 m) were collected with calibration standards interspersed every ten spectra. The FieldSpec FR was reoptimized after spectrum 133 and 200. Photography and cartography were later used to relate the field spectra to relevant hydrologic and geologic features (Fig. 3).

We also collected field spectra for spectrally homogeneous, spatially extensive sites to support further atmospheric calibration of the Hymap hyperspectral data. We collected gridded data in three large flat mine tailing areas, each covering several 1000 m^2 and consisting of 39, 24, and 38 spectra respectively.

5.1. Method of linear unmixing of intermediate-scale gridded data

Understanding the spatial distribution of mineralogy at the landscape scale is essential to scale mineral iden-

tification from hand sample to orbital scales. We analyzed the 20 m × 20 m grid pattern at Anabel's Garden (Fig. 3) to identify the mineralogy and then draw connections between mineralogy and stream character or water chemistry.

Linear mixture modeling is useful for identifying dominant spectral endmembers and their spatial association from a complex scene. The model assumes that the reflectance spectrum of a mixture is a linear combination of independent spectral components [30]. This premise holds if the components are spatially distinct; if they are intimately mixed, photons interact with more than one component during scattering and produce a spectrum that is a nonlinear combination of the components [27].

A linear unmixing from 0.35–1.8 µm with scene-derived endmembers was performed (Fig. 4). This wavelength region was chosen for its ability to distinguish iron oxide and sulfate mineralogy and its high spectral fidelity. First, a zero reflectance and a bright spectrum were linearly unmixed to account for albedo variations. Subsequent scene endmembers were added one at a time to account for spatially coherent areas of high root mean square error (RMS) from the previous unmixing. This process was continued until spectra with high RMS were not sufficiently different from existing endmembers to warrant addition of another endmember. A linear mixing model results in fraction images of the percent of each endmember constituent in each spectrum of the scene. We do not derive mineral percent abundance with this technique because the scene-derived endmembers are not pure minerals and are estimates of a nonlinearly mixed scene. However, we can track both the overall spectral diversity of the scene and how the spectral strength of a constituent, representing a mineral assemblage, varies with distance from the stream.

5.2. Results from linear unmixing of intermediate-scale gridded data

Fraction images and RMS from a seven endmember linear unmixing process over 0.35–1.8 µm and the corresponding endmember spectra are shown in Fig. 4. Endmember naming is a convention and does not represent precisely the endmembers' mineralogy. The two vegetation endmembers are correlated with the two stream types, an expected result since the microbiology and opacity differs between the two streams. The "gypsum" endmember is correlated to the green stream, suggesting that the physiochemical parameters of the green stream lend themselves to gypsum precipitation. The "rozenite" endmember was a major component of only a handful of spectra distributed furthest from the
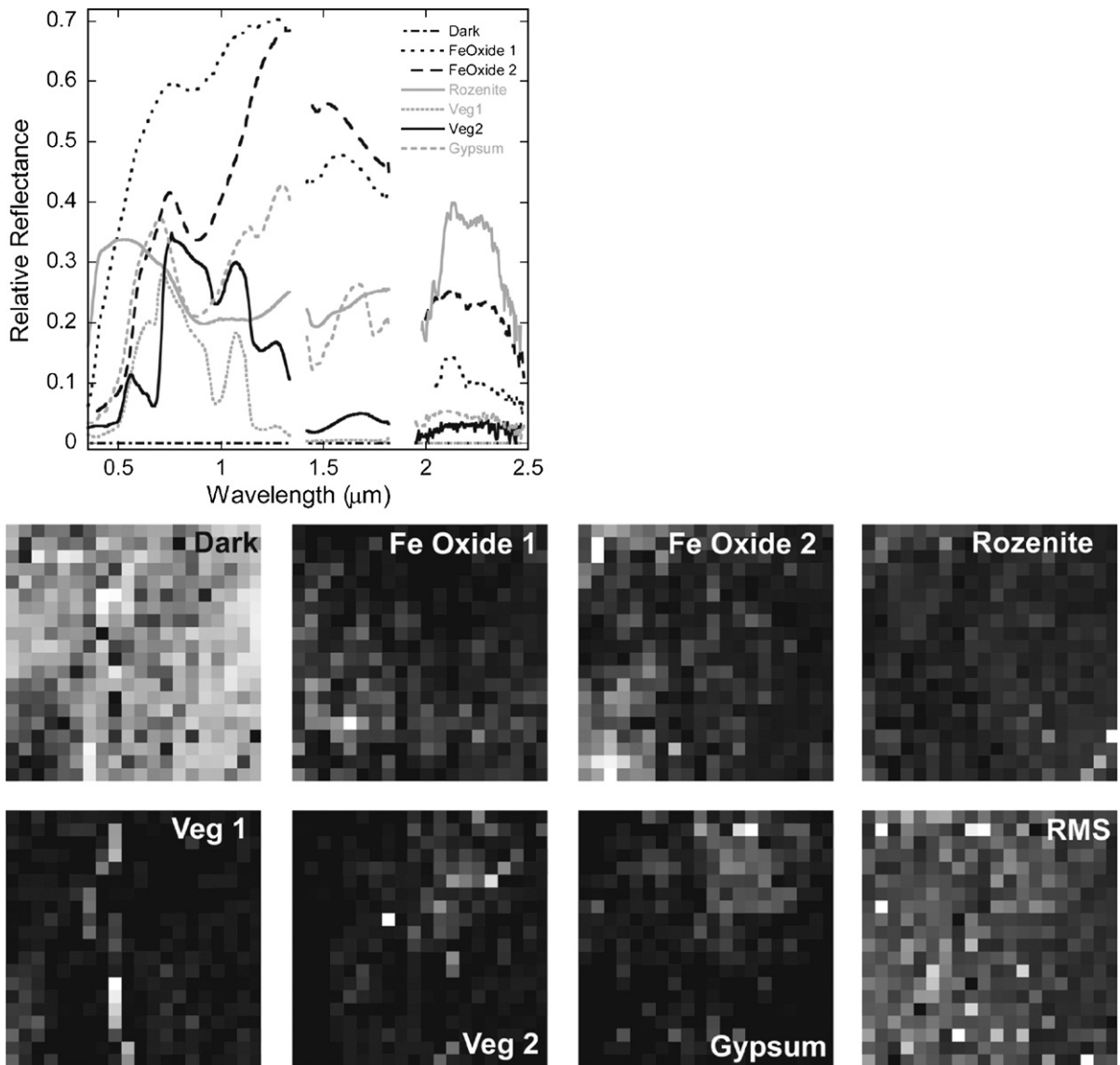
Fig. 4. Anabel's Garden linear unmixing model from gridded field spectra. Fraction images cover the same area and orientation as Fig. 3, a schematic map of Anabel's Garden. Endmembers spectra, fraction images, and RMS for seven endmember linear mixture model over 0.35–1.80 μm. All fraction images scaled 0–1. RMS scaled 0–0.014. The names are for simplicity and are not representative of the entire mineralogy of each endmember.

stream. After identifying seven endmembers in the unmixing model, further endmembers were not added because all areas with high RMS (19 pixels with >0.015) were spectrally very similar to already chosen endmembers. This scene has such diverse mineralogy within 400 spectra that unmixing cannot identify all minerals present.

6. Remotely acquired spectra

Integrated Spectronics collected and calibrated two Hymap scenes over Rio Tinto, Spain on Aug 14, 2004 between 9:07–9:19 UTC. The Hymap instrument is an Australian aerial hyperspectral spectrometer with 61.3° FOV, an IFOV of 2.5 mrad along track and 2.0 mrad across track giving a spatial resolution of 8 m for the Rio Tinto data, and 126 bands covering the 0.45–2.5 μm region. We remove the 1.32–1.44 μm and 1.78–1.97 μm wavelength ranges from analysis because of atmospheric contamination. We employ an empirical line calibration with field spectra collected from spatially extensive and spectrally uniform mine tailings to refine the calibration of the reflectance data [28]. An

empirical line calibration matches remotely acquired data to in situ spectra to correct for the atmospheric contribution in remotely acquired spectra. This calibration works best when in situ spectra are collected from large homogenous surfaces. Our calibration targets were large ochre, black and gray tailing piles (Fig. 1) which each covered a minimum of 25 pixels in the Hymap data.

The mosaicked Hymap scene includes components of vegetation, water and urban areas in addition to the mine tailings and exposed soils. Spectra dominated by vegetation, water and urban land covers are not mineralogically relevant and are masked using the following criteria: spectra with a reflectance value at 1.6 μm less than 0.06 were considered water, spectra with a Normalized Difference Vegetation Index (NDVI) >0.23 were classified as vegetation, and urban areas were masked by defining polygons around them. NDVI quantifies the difference in reflectance between the visible (0.66 μm) and near IR (0.78 μm) channels, which is characteristic of vegetation as chlorophyll strongly absorbs in the visible and is very reflective in the near IR. Spectra with anomalously high or erratic reflectance values were also isolated and excluded. Fig. 5B presents the resulting Hymap data of bare soil and bedrock sur-

rounding Rio Tinto. It is noteworthy that the riverbanks can be distinguished almost along the entire length of the scene, so we are able to study the mineralogy along the river from remotely sensed spectra.

6.1. Method of mineral identification

The abundance of remote sensing data creates a need to reduce spectral and spatial dimensionality for rapid mineral identification. One approach is to identify the most extreme remotely sensed spectra within a region and assume they represent the range in mineralogy present. To isolate extreme remotely sensed spectra, we first perform a Minimum Noise Fraction (MNF) transformation to reduce the spectral dimension of the data [29,30] followed by a Pixel Purity Index (PPI) analysis [31]. The MNF transformation estimates the measurement noise by looking at differences in reflectivity among pixels of a deep lake with low reflectance and homogeneous properties (Fig. 1). It then distributes that noise equally throughout the data. The noise estimate is based on the assumption that adjacent spectra have highly correlated signal but weakly correlated noise [32]. After an MNF transformation, the spatial dimensionality of the data is reduced by extraction of ∼250 extreme
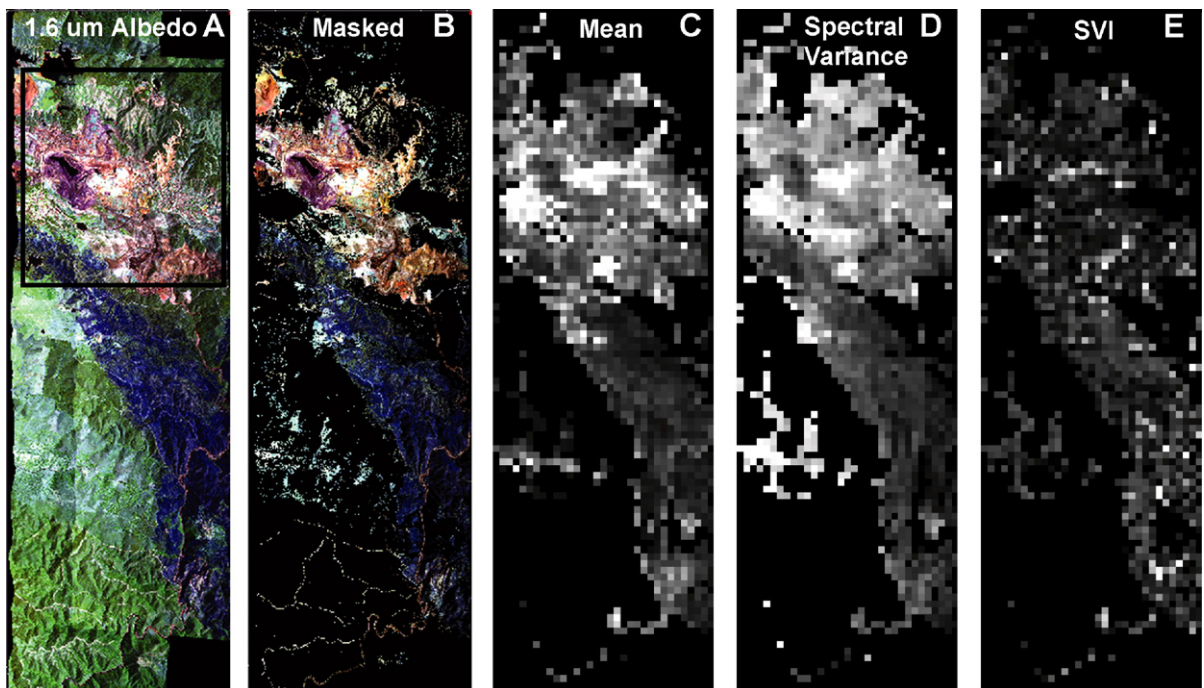

Fig. 5. (A) Albedo map of upper Rio Tinto as seen in Hymap data at 1.6 μm band. (B) Bedrock and bare soil at 1.6 μm. Vegetation, water and urban areas were masked based on criteria such as NDVI, low reflectance at 1.6 μm and polygons outlining urban land cover, respectively. (C) Mean, (D) spectral variance and (E) spectral variance index within 25×25 pixel cells. Context box on (A) shows extent of Fig. 1. Black areas in these maps indicate cells with too few unmasked pixels for analysis.

pixels with the Pixel Purity Index (PPI) function [31]. Enough pixels are chosen to permit classification by spectral character while still being a fraction of the original data volume. All computation was performed with the ENVI software package. We then manually classify the ~250 most spectrally pure pixels and plot all spectra within each class to ensure relatively homogeneous classification. Representative spectra from each class are then analyzed for the number, position and strength of absorption bands which are used to query spectral libraries for mineral identification.

The remotely sensed spectra are separately processed with the MNF, PPI, and n-Dimensional Visualizer functions over the 0.515–2.4 μm wavelength region. Vegetation, urban and water spectra are not masked out of the scene, with the effect that ~40% of ~250 most extreme spectra from each PPI are located in urban or vegetated areas. We perform this analysis with un-masked data because we want to isolate the most extreme spectra, regardless of their land cover type. Grouping into spectral classes is also easier when urban, water and vegetation spectra are included in the analysis since they are so dissimilar from mineralogic spectra that they are always categorized into distinct classes.

6.2. Method of spectral variance index

This section details the method to look for areas with a high concentration of differing spectra that can indicate mineralogically rich and varied regions. The Spectral Variance Index (SVI), adapted from [16], quantifies the amount of spectral variance in each 40,000 m^2 area in the Hymap data. We divide the remotely sensed data into 25×25 pixel (200 m $\times$ 200 m) cells and calculate the average mean (albedo) and spectral variance over all wavelengths for each cell. We next calculate the expected variance for each cell with a linear regression between mean and spectral variance. The standard deviation of the variances also increases with increasing albedo (Fig. 6a) due to the expanded dynamic range and higher intrinsic spectral variance. We account for this relationship by dividing the data into 10 increments of albedo with equal numbers of spectra in each (Table 2) and computing the standard deviation of each cell's spectral variances from its expected variance within each increment. SVI, the number of standard deviations a cell's variance is from its expected variance, is an indicator of how likely it is that a cell's spectral variance can be explained by its albedo. Those
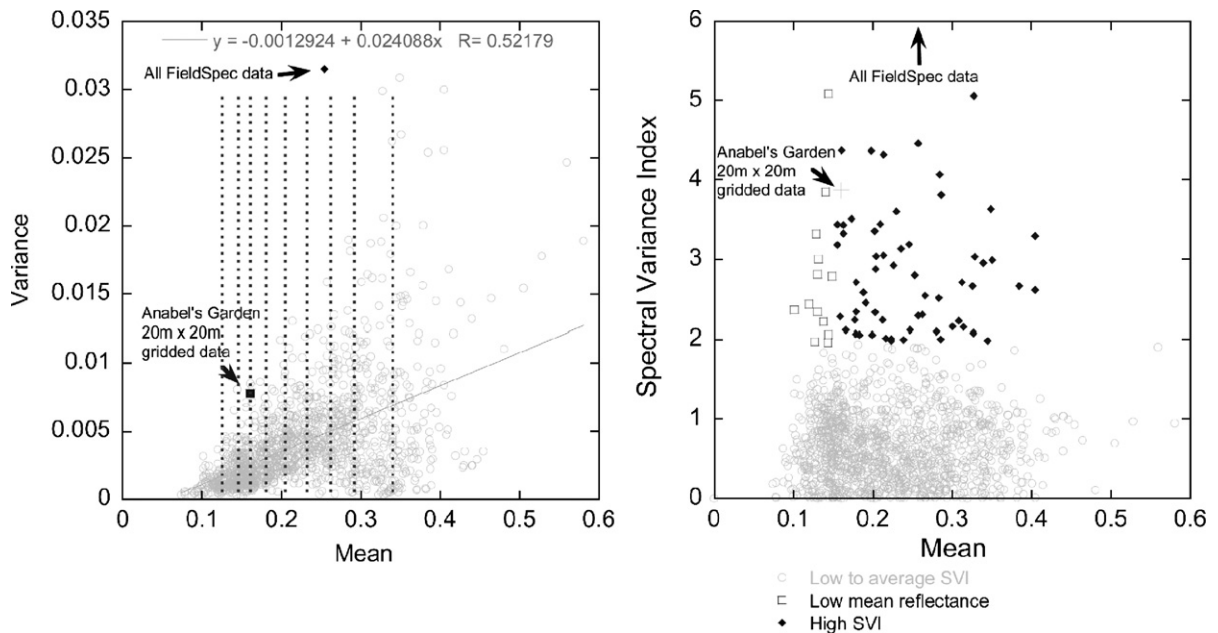

Fig. 6. (a) Scatter plot of spectral variance vs. albedo in each cell in the Hymap remotely sensed data. The dependence of spectral variance on albedo is shown with the linear regression: $y = -0.0012924 + 0.024088$ x, $R = 0.52179$. For comparison, the mean and variance of all the FieldSpec data collected (except Anabel's Garden) and the Anabel's Garden 20 m $\times$ 20 m gridded data are also plotted. There are 406 point spectra each with ~1 cm^2 FOV in the FieldSpec data, and there are 400 point spectra from the 20 m $\times$ 20 m grid of Anabel's Garden, each with ~700 cm^2 FOV. (b) Scatter plot of the Spectral Variance Index vs. albedo for each cell in the Hymap remotely sensed data. Cells with a high spectral variance index and average to high albedo are targets for future exploration as they have more variability than can be explained by just the albedo. That extra variability might be due to mineral diversity. The SVI of the 20 m $\times$ 20 m gridded data at Anabel's Garden (+symbol) is 3.87. The SVI of all the FieldSpec data (10.89) is too high to plot on this figure.

Table 2
Standard deviation of spectral variance in ten increments of albedo

Increment	Albedo range	Std. Dev. of variance
1	<0.132	0.0008574
2	0.132–0.149	0.0011603
3	0.149–0.163	0.001355
4	0.163–0.183	0.001639
5	0.183–0.206	0.0018816
6	0.206–0.233	0.0021316
7	0.233–0.260	0.0024578
8	0.260–0.290	0.003297
9	0.290–0.335	0.004613
10	>0.335	0.006547

cells whose spectral variances are more than two standard deviations from the expected variance have more spectral variance than can be explained by their albedo; other factors, like mineral diversity, must also be invoked to explain the high SVI. These cells are highlighted as potentially mineralogically diverse areas.

Because we are only interested in mineralogic variation, we exclude pixels with vegetation, water or urban land covers from the analysis using the mask described in Section 6. We also exclude cells that had fewer than 100 spectra (∼16% of the area) after applying the mask, because we wanted enough spectra for computations to have statistical relevance.

To test the efficacy of the SVI method to identify mineral diversity, we calculate the mean and SVI for the gridded Anabel's Garden data and for all of the FieldSpec

data collected (except for the gridded Anabel's Garden data). There are 400 spectra in the Anabel's Garden grid and 406 spectra in the rest of the FieldSpec data. Aggregating each of those sets of spectra creates cells with comparable number of spectra to the Hymap cells.

6.3. Results of mineral identification

Representative spectra of seven classes representing iron oxides (Fig. 7A) and sulfates (Fig. 7B). About 25% of the extreme pixels from the PPI analyses of each wavelength region had non-mineralogic spectra – photosynthetic and non-photosynthetic vegetation, urban and water – and were not plotted in Fig. 7. The mineralogy detected in Hymap spectra may differ from that in our field spectra as Hymap data was collected in the dry season and the fieldwork completed during the wet season. Efflorescent minerals are very sensitive to humidity, and their presence and abundance may vary seasonally. Although we do identify spectrally pure pixels, mineral mixing is common at this spatial scale. An example of hematite/phyllosilicate mixing is seen both spectra [142, 650] and [499, 270] in Fig. 7A. We do not present the full range of phyllosilicates identified in Hymap data.

6.4. Results of spectral variance index

Fig. 5 shows graphically the steps performed in the SVI method. Fig. 5A is a 1.6 μm albedo image of the
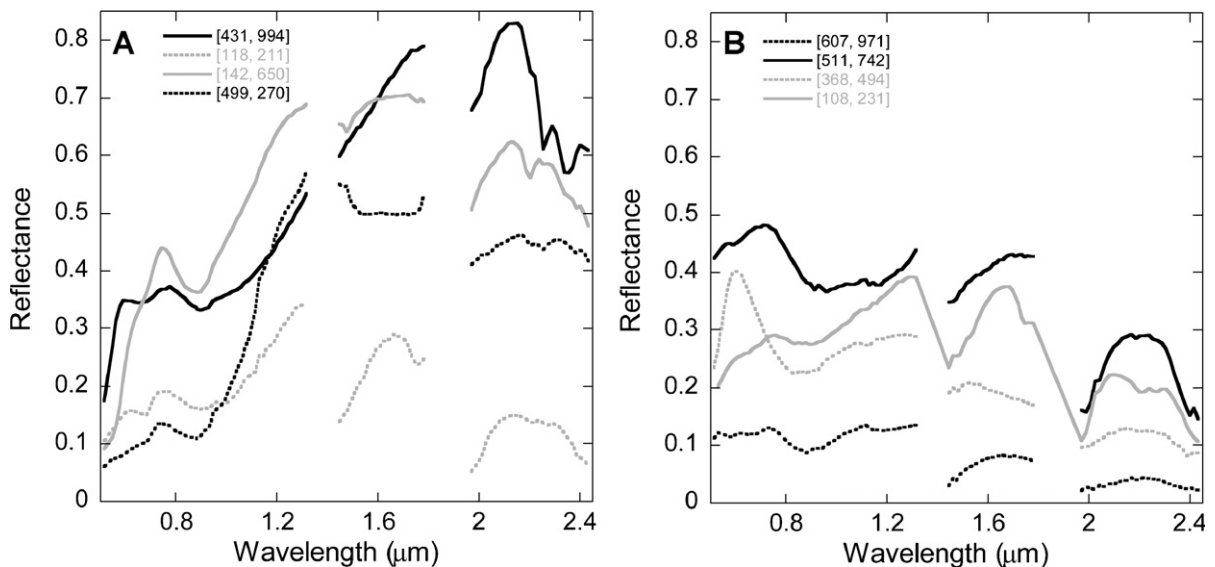

Fig. 7. Representative Hymap spectra of classified (A) iron oxides and (B) mixed hydrated iron sulfates. Spectral classification of extreme Hymap pixels isolated by performing MNF, PPI and n-Dimensional Visualizer functions in ENVI over the 0.515–2.40 μm region. Many of the spectra are hydrated, indicated by visible "wings" of the 1.4, 1.9 and 2.5 μm H_2O absorptions. The 1.4 and 1.9 μm absorptions cannot be quantified due to the effect of atmospheric H_2O.

Rio Tinto basin. A box outlines the extent of Fig. 1 and our locations of sample collection. Fig. 5B masks all but bedrock and soil exposes. Fig. 5C–E shows the binned mean albedo, spectral variance, and spectral variance index value. As discussed before, a scatter plot of the spectral variance of each cell vs. its albedo has a distinct wedge shape (Fig. 6a). The expected variation is given by the best-fit line: $y = -0.001292 + 0.024088$ x.

Plotting the SVI vs. albedo is informative to understanding how SVI works (Fig. 6b). Most cells are clustered in at low SVI values — this is reasonable because the majority of cells have minimal spectral diversity. Cells that have an SVI greater than 2.0 are partitioned into two categories. The first category contains those cells with high SVI and a low albedo. Spectra with low albedos have less dynamic range and generally have intrinsically lower spectral variance than spectra with higher albedos. However, the addition of a few spectra with high albedo can significantly increase the spectral variance. Analysis of the spectra in cells in the first category show they do indeed have high variation in their spectra, but the mineralogic interpretation shows burned vegetation, bare soil, low albedo iron oxide, and low signal-to-noise spectra with a couple of brighter spectra to increase variance. While appropriately identified as diverse, we are interested in different properties.

The second category contains cells characterized by high SVI and an arbitrarily high albedo (Fig. 5E) that are targets for future exploration. Based on scene analysis, locations of high SVI with an albedo below ~0.15 were not associated with real mineralogical diversity. They are clustered in the tailings region and could indicate exposures of mineralogically diverse sediments. A couple of the cells are located along the river, further downstream of the tailings. The riverbanks widen here, perhaps allowing enough signal from the iron oxide mineralogy present in the riverbanks to be included in the analysis that its diversity becomes significant.

7. Discussion

A high diversity of iron oxide and sulfate minerals are observed in situ at high spatial resolution. Our determination of mineralogy using VNIR spectroscopy and elemental chemistry is consistent with previous studies that documented the evolution in mineralogy using XRD and Mössbauer spectroscopy [e.g. 4,8] and shows this environment is well characterized by VNIR reflectance spectroscopy. VNIR spectroscopy is an important part of an exploration strategy as it can identify the abundance and diversity of mineralogy over a variety of spatial scales and provides essential context

when considering the mineralogic signatures of habitability [5].

This study also shows that changes in mineralogy with diagenesis that indicate trends in mineral stability [25,33] can be resolved with VNIR spectroscopy. Iron sulfates and oxides such as schwertmannite, jarosite, and rozenite, are found in the recent sediments along Rio Tinto. These minerals dehydrate and become leached into goethite and hematite in the abandoned river terraces. The three terraces vary in age but all have similar mineralogy and elemental compositions, suggesting that the mineralogy converges to a stable configuration. Comparing the mineralogy of recent sediments and the lithified terraces illustrates an evolution with time from diverse to homogeneous mineralogy. We might be able to use this directional mineral collection to recognize Rio Tinto-like environments on Mars in various stages of diagenesis.

Efflorescent copiapite on top of hematite-rich deposits was another weathering trend noticed at several locations in Rio Tinto recent sediments and tailing piles. Upon precipitation, Fe^{2+} sulfates start to desiccate and oxidize, converting to mixed ferrous–ferric sulfates, then to hydrous ferric oxides, and ultimately to hematite [33]. Desiccation does not change the popcorn-like morphology between the copiapite and hematite deposits. Copiapite is a common mineral along a directional path of desiccation and oxidation from melanterite to goethite [33]. Similar combinations could be found on Mars, with sulfates overlaying iron oxides. The desiccation/oxidation process might have been halted before going to completion. Using VNIR signatures to identify Rio Tinto-like mineral combinations could be important for Mars exploration.

When looking at landscape scale spectra, as in the 20 m×20 m grid at Anabel's Garden, we noted the mineral distribution was associated with distance from the stream and is a function of the dynamic stream geochemistry and biological interactions. There is somewhat reduced diversity in the gridded data compared to point spectra collected elsewhere due to the decreased spatial resolution, but the mineral diversity is still high. A linear mixture model approximates the mineral diversity at Anabel's Garden and its spatial distribution, even though the assumption of linear mixing is less robust as efflorescent sulfates occur in both spatially distinct patterns and in intimate mixtures with the soils.

We identify seven endmembers in a linear unmixing model of Anabel's Garden. While the endmembers are not themselves pure minerals and do not represent all of the minerals present, they indicate the diversity and abundance of mineralogy present. Iron oxides are ubiquitous, "gypsum" is concentrated along margins of the

more reduced stream, and "rozenite" is only identified as the dominant endmember in pixels far from the stream. This distribution is expected because sulfates are very soluble efflorescent minerals that form via capillary action and evaporation in acid mine drainage areas [7].

To test the applicability of the SVI technique to Rio Tinto mineralogy, we run several comparisons. First, we compare the SVI values to the mineralogy detected in the field for two cells where we also had identified the mineralogy over a spatially extensive area: Anabel's Garden and the broad, flat ochre mine tailings pile. The sensitivity of the SVI to mineral diversity is tested by computing the SVI value of landscape scale gridded field spectra of Anabel's Garden and of all of the field spectra except for the Anabel's Garden gridded data (Fig. 6b).

Comparison of the SVI values to the mineralogy detected in the field at Anabel's Garden and the ochre tailings yielded consistent results. Areas near Anabel's Garden have high SVI values (2.89 and 3.37) and are located proximal to the Rio Tinto source springs, which are the areas with the most diverse mineralogy in field analyses. Anabel's Garden itself did not show up as having a high SVI, but that might be attributable to its small spatial extent; it might not have covered enough pixels to contribute significantly to its cell's SVI. The Hymap data was collected during the dry season while our fieldwork was completed in the wet season; seasonal changes in both the mineral diversity and abundance are also a complicating factor. The cell that consisted entirely of ochre tailing spectra had a very low SVI value (0.96). Comparison to field spectra show that the area is very spectrally uniform with a low spectral variance. The spectra show deep but consistent absorption features due to the presence of goethite.

Since there is greater spatial resolution in the Anabel's Garden cell, we expect them to be greater spectral diversity (minerals are better resolved and spectra show less mineral mixing) and hence a higher SVI than the comparable Hymap spectra. The rest of the FieldSpec data is at even higher spatial resolution, and many spectra are mono-mineralic. This should result in a suite of very diverse spectra. We expect an even higher SVI from the aggregated FieldSpec data than the gridded Anabel's Garden data. As expected, the Anabel's Garden grid from field data has a mean of 0.1603 and an SVI of 3.87 while the FieldSpec data (except the Anabel's Garden data) has a mean of 0.254 and an SVI of 10.89.

The spatial approach for computing the SVI also includes unwanted effects for albedo differences and boundaries between spectral units. For example, a cell that contains two spectrally uniform areas and a sharp boundary between the two might evaluate to a high SVI because the two units are spectrally distinct enough to create high variance at each wavelength. In this case, a cell with low mineral diversity can have a high SVI value. Other, non-mineralogic factors that can strongly affect the SVI value of a given cell are the presence of water, buildings and vegetation.

Both our ability to distinguish unique mineral signatures and to recognize sub-pixel spectral diversity is predicated on the spectral expression of interesting mineralogy in data traversing several spatial scales. Spatially coarse spectra might have too much mineral mixing to identify the specific mineralogy present. Areas with diverse mineralogy might be too small to significantly affect the SVI value in a cell. However, when the area of high spectral variance is large enough, there is enough information in spatially coarse spectra to resolve them. SVI can detect young and diverse mineralogy in close association in Rio Tinto-like environments. The SVI creates a symbiosis between spectra of different spatial resolutions, taking advantage of the large-scale mapping ability from remotely sensed spectral and the mineral identification ability from field spectra.

8. Conclusions

VNIR spectroscopy indicates an iron oxide and sulfate assemblage at Rio Tinto at the hand sample, landscape and orbital scales in various stages of maturity. Recent sediments show more mineral diversity than ancient river terraces, which have been leached of their sulfates. Elemental abundance analyses support the spectral determination that the terraces are dominantly iron oxide. The presence of efflorescent sulfates is linked with distance from stream; during the wet season, spectra consistent with rozenite occur about 5 m from the stream while gypsum-like spectra indicate a stable presence right at the margins of a reduced stream.

There has been an implicit understanding in the literature that decreasing spatial resolution decreases the ability to identify mineralogy. This paper is the first known quantitative study of spatial scaling on detecting concentrations of diverse mineralogy. We apply the SVI to the iron oxide and sulfate-rich mineralogy of Rio Tinto, but the same technique can be used in other environments with an abundant and varied mineralogy. This technique is powerful when sifting through large spectral datasets and has the potential to revolutionize remotely acquired hyperspectral data analysis. The SVI method can search global or regional datasets to find mineralogically diverse environments, not by matching spectral shape but by the characteristic variability of a

cluster of spectra themselves. Locating concentrations of diverse mineralogy from orbital data, such as OMEGA or CRISM (Compact Reconnaissance Imaging Spectrometer for Mars) [34], is important for exploring Rio Tinto-like environments on Mars. These areas could represent loci of mineral formation processes and are key targets to further investigate at higher spatial scale with rovers or landers, such as the Mars Science Laboratory. With limited resources for ground investigations to cover large distances, landings sites must be chosen to maximize opportunities for science discovery within a small confine.

Acknowledgements

References

[1] E. Gónzalez-Toril, E. Llobet-Brossa, E.O. Casamayor, R. Amann, R. Amils, Microbial ecology of an extreme acidic environment, the Tinto River, Appl. Environ. Microbiol. 69 (2003) 4853–4865.

[2] A.I. López-Archilla, I. Marín, A. González, R. Amils, Microbial community composition and ecology of an acidic aquatic environment, Microb. Ecol. 41 (2001) 20–35.

[3] L.A. Amaral-Zettler, F. Gómez, E. Zettler, B.G. Keenan, R. Amils, M. Sogin, Eukaryotic diversity in Spain's River of Fire, Nature 417 (2002) 137.

[4] D.C. Fernández-Remolar, R.V. Morris, J.E. Gruener, R. Amils, A.H. Knoll, The Río Tinto Basin, Spain: mineralogy, sedimentary geobiology and implications for interpretation of outcrop rocks at Meridiani Planum, Mars, Earth Planet. Sci. Lett. 240 (2005) 149–167, doi:10.1016/j.epsl.2005.09.043.

[5] D.C. Fernández-Remolar, J. Gómez-Elvira, F. Gómez, E. Sebastian, J. Martíín, J.A. Manfredi, J. Torres, C. González Kesler, R. Amils, The Tinto River, an extreme acidic environment under control of iron, as an analog of the Terra Meridiani hematite site of Mars, Planet. Space Sci. 52 (2004) 239–248.

[6] C.A. Boulter, Comparison of Rio Tinto, Spain, and Guaymas Basin, Gulf of California: an explanation of a supergiant massive sulfide deposit in an ancient sill-sediment complex, Geology 21 (1993) 801–804.

[7] T. Buckby, S. Black, M.L. Coleman, M.E. Hodson, Fe-sulphate-rich evaporative mineral precipitates from the Rio Tinto, southwest Spain, Mineral. Mag. 67 (2003) 263–278.

[8] S. Chemtob, Efflorescent Sulfates at Rio Tinto, a Mars Analog Terrain: Phase Identification by Raman and Reflectance Spectroscopy, Undergraduate Thesis, Washington University in St. Louis (2006).

[9] F. Rull, J. Martinez-Frias, J. Medina, Surface mineral analysis from two possible Martian analogs (Rio Tinto and Jaroso Ravine, Spain) using micro-, macro-, and remote laser Raman spectroscopy, Geophys. Res. Abstr. 7 (2005).

[10] P.R. Christensen, J.L. Bandfield, R.N. Clark, K.S. Edgett, V.E. Hamilton, T. Hoefen, H.H. Kieffer, R.P. Kuzmin, M.D. Lane, M.C. Malin, R.V. Morris, J.C. Pearl, R. Pearson, T.L. Roush, S.W. Ruff, M.D. Smith, Detection of crystalline hematite mineralization on Mars by the Thermal Emission Spectrometer: evidence for near-surface water, J. Geophys. Res. 105 (2000) 9623–9642.

[11] P.R. Christensen, M.B. Wyatt, T.D. Glotch, A.D. Rogers, S. Anwar, R.E. Arvidson, J.L. Bandfield, D.L. Blaney, C. Budney, W.M. Calvin, A. Fallacaro, R.L. Fergason, N. Gorelick, T.G. Graff, V.E. Hamilton, A.G. Hayes, J.R. Johnson, A.T. Knudson, H.Y. McSween Jr., G.L. Mehall, L.K. Mehall, J.E. Moersch, R.V. Morris, M.D. Smith, S.W. Squyres, S.W. Ruff, M.J. Wolff, Mineralogy at Meridiani Planum from the Mini-TES experiment on the Opportunity Rover, Science 306 (2004) 1733–1739.

[12] C. Klingelhöfer, R.V. Morris, B. Bernhardt, D.S. Rodionov, P.A. de Souza Jr., A. Yen, R. Gellert, E.N. Evlanov, B. Zubhov, J. Foh, U. Bonnes, E. Kankeleit, P. Gutlich, D.W. Ming, F. Renz, T. Wdowiak, S.W. Squyres, R.E. Arvidson, Jarosite and Hematite at Meridiani Planum from Opportunity's Mössbauer Spectrometer, Science 306 (2004) 1740–1745.

[13] J.-P. Bibring, Y. Langevin, A. Gendrin, B. Gondet, F. Poulet, M. Berthé, A. Soufflot, R. Arvidson, N. Mangold, J. Mustard, P. Drossart, the OMEGA team, Mars Surface Diversity as Revealed by the OMEGA/Mars Express Observations, Science 307 (2005) 1576–1581.

[14] J.-P. Bibring, Y. Langevin, J.F. Mustard, F. Poulet, R. Arvidson, A. Gendrin, B. Gondet, N. Mangold, P. Pinet, F. Forget, the OMEGA team, Global mineralogical and aqueous mars history derived from OMEGA/Mars Express Data, Science 312 (2006) 400–404.

[15] F.A. Kruse, Geologic mapping using combined analysis of Airborne Visible/Infrared Imaging Spectrometer (AVIRIS) and SIR-C/X-SAR Data, Proc., Int. Symp. Opt. Sci., Eng., Instrum., SPIE Proc., Denver 2819 (1996) 24–35.

[16] S. Martínez-Alonso, M.T. Mellon, B.C. Kindel, B.M. Jakosky, Mapping compositional diversity on the surface of Mars: the spectral variance index, J. Geophys. Res. 111 (2006), doi:10.1029/2005JE002492.

[17] D. Fernández-Remolar, O. Prieto-Ballesteros, C. Stocker, Searching for an acidic aquifer in the Río Tinto Basin: First geobiology results of MARTE project, Lunar Planet. Sci. Conf. XXXV, 2004 abstract #1766.

[18] C.M. Pieters, Strength of mineral absorption features in the transmitted component of near-infrared reflected light: first results from RELAB, J. Geophys. Res. 88 (B11) (1983) 9534–9544.

[19] C.M. Pieters, T. Hiroi, RELAB (Reflectance Experiment Laboratory): A NASA Multiuser Spectroscopy Facility, Lunar Planet. Sci. Conf. XXXV, 2004 abstract #1720.

[20] J.F. Mustard, C.M. Pieters, Quantitative abundance estimates from bidirectional reflectance measurements, J. Geophys. Res. 92 (B4) (1987) E617–E626.

[21] R.G. Burns, Mineralogical Applications of Crystal Field Theory, 2nd ed. Cambridge University Press, New York, 1993.

[22] R.N. Clark, G.A. Swayze, R. Wise, K.E. Livo, T.M. Hoefen, R.F. Kokaly, S.J. Sutley, USGS Digital Spectral Library splib05a, USGS Open File Report, vol. 03–395, 2003.

[23] R.N. Clark, Spectroscopy of rocks and minerals, and principles of spectroscopy, in: A.N. Rencz (Ed.), Remote Sensing for the Earth Sciences: Manual of Remote Sensing, Wiley, New York, 1999, pp. 3–58.

[24] J.L. Bishop, E. Murad, The visible and infrared spectral properties of jarosite and alunite, Am. Mineral. 90 (2005) 110–1107.

[25] J.L. Jambor, D.K. Nordstrom, C.N. Alpers, Metal-sulfate salts from sulfide mineral oxidation, in: C.N. Alpers, J.L. Jambor, D.K. Nordstrom (Eds.), Reviews in Mineralogy and Geochemistry: Sulfate Minerals, Mineralogical Society of America, Washington, DC, 2000, pp. 303–350.

[26] E.A. Cloutis, F.C. Hawthorne, S.A. Mertzman, K. Krenn, M.A. Craig, D. Marcino, M. Methot, J. Strong, J.F. Mustard, D.L. Blaney, J.F. Bell III, F. Vilas, Detection and discrimination of sulfate minerals using reflectance spectroscopy, Icarus 184 (2006) 121–157.

[27] P. Switzer, A.A. Green, Min/max autocorrelation factors for multivariate spatial imagery, Dept of Statistics, Stanford University, Technical Report, vol. 6, 1984.

[28] G.M. Smith, E.J. Milton, The use of the empirical line method to calibrate remotely sensed data to reflectance, Int. J. Remote Sens. 20 (1999) 2653–2662.

[29] J.L. Bishop, M.D. Dyar, M.D. Lane, J.F. Bandfield, Spectral identification of hydrated sulfates on Mars and comparison with acidic environments on Earth, Int. J. Astrobiol. 3 (2004) 275–285.

[30] A.A. Green, M. Bereman, P. Switzer, M.D. Craig, A transformation for ordering multispectral data in terms of image quality with implications for noise removal, IEEE Trans. Geosci. Remote Sens. 26 (1988) 65–74.

[31] J.W. Boardman, F.A. Kruse, Automated spectral analysis: a geologic example using AVIRIS data, north Grapevine Mountains, Nevada, Proc. 10th Themat. Conf. Geol. Remote Sens., vol. 1, Environmental Research Institute Michigan, 1994, pp. 407–418.

[32] J.W. Boardman, F.A. Kruse, R.O. Green, Mapping target signatures via partial unmixing of AVIRIS data, Summ. 5th Annual JPL Airborne Earth Sci. Work, vol. 1, 1995, pp. 23–26.

[33] J.K. Jerz, J.D. Rimstidt, Efflorescent iron sulfate minerals: paragenesis, relative stability, and environmental impact, Am. Mineral. 88 (2003) 1919–1932.

[34] S. Murchie, et al., CRISM (Compact Reconnaissance Imaging Spectrometer for Mars) on MRO (Mars Reconnaissance Orbiter), J. Geophys. Res. (in press).

[35] M.D. Lane, M.D. Dyar, J.L. Bishop, Spectroscopic evidence for hydrous iron sulfate in the Martian soil, Geophys. Res. Lett. 31 (2004), doi:10.1029/2004GL021231.